Modeling Heterogeneous Melting in Phase Change Memory Devices

J. Scoggin, ¹ Z. Woods, ¹ H. Silva, ¹ and A. Gokirmak ¹

¹Department of Electrical and Computer Engineering, University of Connecticut, Storrs, Connecticut 06269, USA

We present thermodynamic crystallization and melting models and calculate phase change velocities in $Ge_2Sb_2Te_5$ based on kinetic and thermodynamic parameters. The calculated phase change velocities are strong functions of grain size, with smaller grains beginning to melt at lower temperatures. Phase change velocities are continuous functions of temperature which determine crystallization and melting rates. Hence, set and reset times as well as power and peak current requirements for switching are strong functions of grain size. Grain boundary amorphization can lead to a sufficient increase in cell resistance for small-grain phase change materials even if the whole active region does not completely amorphize. Isolated grains left in the amorphous regions, the quenched-in nuclei, facilitate templated crystal growth and significantly reduce set times for phase change memory cells. We demonstrate the significance of heterogeneous melting through 2-D electrothermal simulations coupled with a dynamic materials phase change model. Our results show reset and set times on the order of ~1 ns for 30 nm wide confined nanocrystalline (7.5 nm – 25 nm radius crystals) phase change memory cells.

Solids tend to melt heterogeneously: the liquid phase initially forms at high energy sites such as grain boundaries and material interfaces. While many materials heat ~20% above their melting temperature (T_{melt}) before the liquid phase forms within the bulk solid, heterogeneous melting may occur below T_{melt}^{-1} . In this manuscript, we consider the impacts of heterogeneous melting on phase change memory (PCM). PCM is a non-volatile memory technology which stores information as the low resistivity crystalline or high resistivity amorphous phase of a material (Fig. 1). PCM retention, endurance, and speed depend on the physics underlying crystallization and melting. We model temperature and grain size dependent phase change velocities in Ge₂Sb₂Te₅ (GST), a common phase change material, based on kinetic and thermodynamic parameters. We incorporate heterogeneous melting into a finite element phase change model coupled

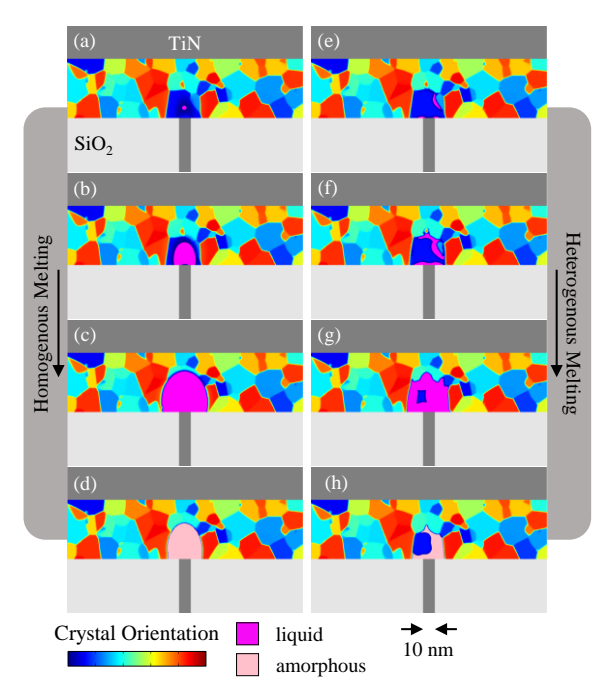


Fig. 1: The crystal-to-amorphous transition in a PCM mushroom cell using (a-d) homogenous and (e-h) heterogeneous melting resulting in a reset-to-initial resistance ratio of ~200 and ~100, respectively.

with electrothermal physics^{2–7} and show that it can account for the experimentally demonstrated PCM performance improvement with decreasing grain size^{8,9}.

 T_{melt} is the temperature at which the Gibbs free energy difference between bulk liquid and crystalline phases (Δg_{lc}) is zero. However, melting becomes thermodynamically favorable below T_{melt} at crystal interfaces. The Gibbs free energy of a spherical crystal surrounded by liquid (ΔG_{crys}) is calculated by classical nucleation theory as

$$\Delta G_{crys} = -\frac{4}{3}\pi r^3 \Delta g_{lc} + 4\pi r^2 \gamma_{lc} , \qquad (1)$$

where r is the crystal radius and γ_{lc} is the energy penalty at a liquid-crystal interface (Fig. 2a). (1) has extrema at r = 0 and $r = r_c$, the critical radius:

$$r_c = \frac{2\gamma_{lc}}{\Delta g_{lc}}. (2)$$

Crystals with $r < r_c$ are subcritical and can reduce ΔG_{crys} by shrinking, i.e. melting. r_c increases with T: Δg_{lc} decreases with increasing T, crossing 0 at T_{melt} . γ_{lc} is difficult to measure in GST and often used as a fitting parameter; however, γ_{lc} increases with T in metals as well as in the semiconductors Si and Ge^{10–14}. Here, we use $\gamma_{lc} = 75$ mJ/m², a temperature-independent value which allows classical nucleation theory to accurately model nucleation and growth in GST over a wide temperature range¹⁵. 1 nm and 10 nm radius GST grains become subcritical at ~640 K and ~840 K, respectively, with

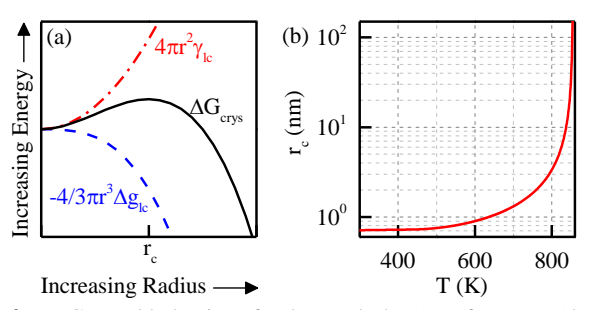


Fig. 2: (a) General behavior of volume (dashes), surface area (dashdots), and total (solid) contributions to the Gibbs free energy of a crystal. (b) r_c increases with T, diverging to infinity at T_{melt} .

the parameters in this work (Fig. 2b).

Grain boundary melting may be thermodynamically favorable below T_{melt} (pre-melting) even for supercritical grains $(r > r_c)$ if

$$2\gamma_{lc} + w\Delta g_{lc} < \gamma_{cc},\tag{3}$$

where w is the width of liquid formed and γ_{cc} is the crystalline-crystalline interface (grain boundary) energy penalty. Not all grain boundaries pre-melt at the same temperature since γ_{cc} depends on the misorientation between grains, as calculated via phase field crystal simulations and shown experimentally with colloidal crystals While (3) presents a thermodynamic pathway for only a finite w, a supercritical grain may become subcritical while pre-melting and consequently melt entirely.

Regardless of the underlying mechanism, melting is a transient process and requires kinetic and thermodynamic parameters to model. We model phase change velocity (ν) as:

$$v = v_{kinetic} \left(1 - \exp\left(-\frac{\Delta g}{RT} \right) \right) \tag{4}$$

where $v_{kinetic}$ is the kinetic upper limit, R is the gas constant, and Δg is the non-negative thermodynamic driving force. (4) is appropriate for atomically rough interfaces¹⁸, predicts a smooth derivative of v as crystallization transitions to melt at $\Delta g = 0$ ¹⁸, and has been used to model crystallization dynamics in glass formers including GST^{19,20}.

We model $v_{kinetic}$ for GST as in Orava *et.* al^{20} : the temperature dependence is determined from ultra-fast digital scanning calorimetry²⁰, and $v_{kinetic}(900 \text{ K})$ is calculated from

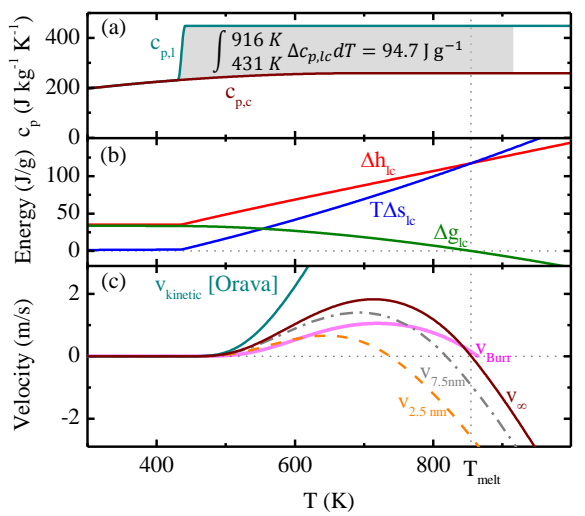


Fig. 3: (a) The integral of $\Delta c_{p,lc}$ accounts for the difference in the latent heats of fusion and crystallization ($\Delta h_{lc}(916 \text{ K}) = 128.9 \text{ J/g}$ and $\Delta h_{lc}(431 \text{ K}) = 34.2 \text{ J/g}$, respectively²²). (b) Calculated thermodynamic parameters. (c) Phase change velocities for bulk, 7.5 nm (dash-dots), and 2.5 nm (dashes) radius grains and that calculated by Burr *et. al*²⁵. Negative values denote melting. $v_{kinetic}$ stabilizes with the liquid viscosity at higher temperatures; $v_{kinetic}(T > 2000 \text{ K}) \approx 60 \text{ m/s}$.

the liquid viscosity given by molecular dynamics simulations ($\eta(900 \text{ K}) \approx 1.1 \text{ mPa s})^{21}$.

We calculate Δg from Δg_{lc} , which is thermodynamically related to the differences in enthalpy (Δh_{lc}) and entropy (Δs_{lc}) between phases:

$$\Delta g_{lc}(T) = \Delta h_{lc}(T) - T \Delta s_{lc}(T). \tag{5}$$

 Δh_{lc} and Δs_{lc} can be calculated from the difference in specific heat between phases ($\Delta c_{p,lc}$):

$$\Delta h_{lc}(T) = \int_0^T \Delta c_{v,lc}(T') dT'$$
 (6a)

$$= \Delta h_{lc}(T_x) + \int_{T_x}^T \Delta c_{p,lc}(T') dT'$$
 (6b)

$$\Delta s_{lc}(T) = \int_0^T \frac{\Delta c_{p,lc}(T')}{T'} dT'$$
 (7a)

$$= \Delta s_{lc} \left(T_y \right) + \int_{T_y}^{T} \frac{\Delta c_{p,lc} (T')}{T'} dT' \tag{7b}$$

where T_x and T_y are temperatures at which Δh_{lc} and Δs_{lc} are known. We treat the amorphous and liquid phases as a single material with a sharp change in thermodynamic parameters at the glass transition temperature ($T_{glass} = 431 \text{ K}^{22}$), neglecting the dependence of these parameters and T_{glass} on thermal history²³. We model liquid and crystalline specific heats such that $\Delta c_{p,lc}$ accounts for the difference in the latent heats of fusion and crystallization⁹ (Fig. 3a). We use $\Delta h_{lc}(916 \text{ K}) = 128.9 \text{ J/g}^{22}$ and $\Delta s_{lc}(T_{melt}) = \Delta h_{lc}(T_{melt})/T_{melt}$ as our known values ($T_{melt} = 855 \text{ K}^{24}$) and calculate $\Delta h_{lc}(T)$, $\Delta s_{lc}(T)$, and $\Delta g_{lc}(T)$ (Fig. 3b). We calculate phase change velocities using Δg_{lc} for bulk (v_{∞}) and Δg_{crys} for crystals with radius $r(v_r)$:

$$\Delta g_{crys} = \Delta G_{crys} \times \frac{m_{GST}}{Vol_r \times d_{GST}}$$
 (8)

where m is molar mass, Vol is volume, and d is mass density. We also use m_{GST} and d_{GST} 8to convert Δg_{lc} from J/g to J/mol before using it in (4). v is a continuous function which changes sign at the size dependent critical temperature (i.e. when $r = r_c$, Fig. 2b), implemented using $\Delta g_{cl} = -\Delta g_{lc}$ (Fig. 3c). Smaller grains are expected to melt faster or crystallize slower. Hence using v_{∞} , as in the simulations below, gives a lower bound for melting and an upper bound for crystallization velocities.

We model heat transfer and current continuity to simulate PCM device operation including thermoelectric effects²⁶:

$$dc_p \frac{dT}{dt} - \nabla \cdot (k\nabla T) = -\nabla V \cdot J - \nabla \cdot (JST) + q_H \quad (9)$$

$$\nabla \cdot I = \nabla \cdot (-\sigma \nabla V - \sigma S \nabla T) = 0 \tag{10}$$

where k is thermal conductivity, V is electric potential, J is current density, S is the Seebeck coefficient, q_H is the latent heat of phase change²⁷, and σ is electrical conductivity.

We model phase change similarly as in Woods *et.* $al^{2,3}$, which we briefly describe here before discussing updates that

capture heterogeneous melting. Woods *et.* $al^{2,3}$ tracks the 3-vector \overrightarrow{CD} with coupled rate equations

$$\frac{dCD_i}{dt} = Nucleation_i + Growth_i + Melt_i.$$
 (11)

The phase of the material (CD) is defined by the sum of components: $CD = \Sigma(CD_i) = 0$ for the amorphous/liquid or 1 for the crystalline phase. Grain orientation is given by the distribution of CD_i values (Fig 4a), with grain boundaries defined where $|\nabla \overrightarrow{CD}| > 5 \times 10^{-3} \text{ nm}^{-1}$. *Nucleation*_i randomly generates nuclei at a temperature dependent rate. *Growth*_i has a stability term $(stbl_i)$ which drives CD to 0 or 1 and a diffusivity term $(diff_i)$ which grows grains outwards:

$$Growth_{i} = stbl_{i} \times \frac{cD_{i}}{cD} + \nabla(diff_{i})\nabla CD_{i}$$

$$stbl_{i} = \alpha_{stbl} \times v(T) \times pw_{stbl}(CD)$$

$$diff_{i} = \alpha_{diff} \times v(T) \times pw_{diff}(CD)$$
(12)

where $\alpha_{stbl} = 0.8 \text{ nm}^{-1}$ and $\alpha_{diff} = -0.2 \text{ nm}$ are constants, pw_{stbl} and pw_{diff} are piecewise control functions (Fig 5), and v is the phase change velocity. A valley in pw_{stbl} prevents small perturbations above 0 from triggering crystallization (Fig 5a inset). Nucleation or templated growth from an adjacent crystal is required to escape this well. $Melt_i$ brings CD_i (and thus CD) to 0 when $T > T_{melt}$:

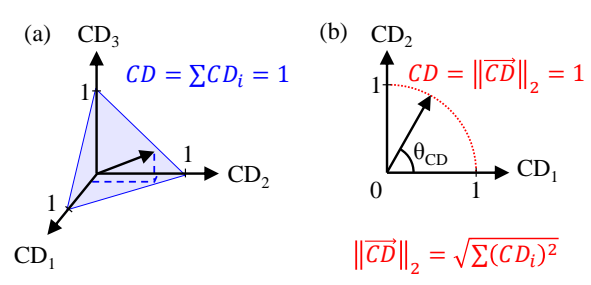


Fig 4. Crystalline vectors defined by (a) a 3-vector with $CD = \Sigma(CD_i)$ as in Woods *et. al*³ and (b) a 2-vector with $CD = ||CD||_2$ as used here. The cut plane and dotted line show allowed crystalline values.

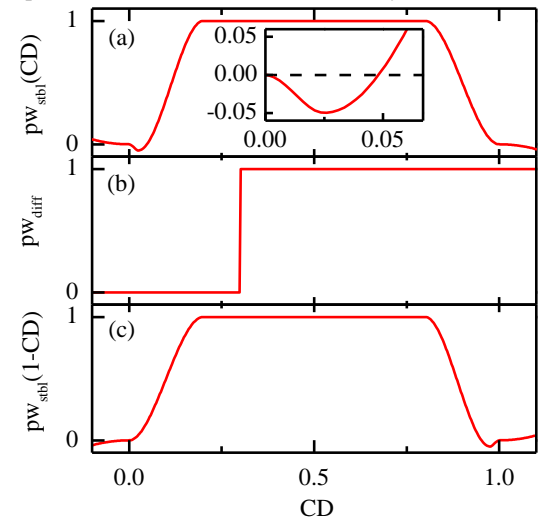


Fig 5. Control functions for (a) $stbl_i$ when $T < T_{melt}$, (b) $diff_i$, and (c) $stbl_i$ when $T > T_{melt}$. A stability well in (a)/(c) prevents small perturbations from triggering crystallization/melt, respectively.

$$Melt_i = \alpha_{melt} \times (T > T_{melt}) \times CD_i$$
 (13)

where $\alpha_{melt} = -1 \text{ ns}^{-1}$ is a constant and $(T > T_{melt})$ is a step function (0 to 1 over a 1 K window centered at T_{melt}).

In this work, we use a 2-vector \overline{CD} , which is sufficient to capture grain boundaries while reducing the number of equations solved. We use $CD = \sqrt{CD_1^2 + CD_2^2}$ instead of $CD = \Sigma(CD_i)$, fixing all crystalline vectors at an equal length in CD-space and ensuring that their lengths approach zero (they melt) at the same rate (Fig 4b). *Nucleationi* generates nuclei with a random angle $(10^\circ \le \theta_{CD} \le 80^\circ)$. θ_{CD} can be mapped to a physical grain orientation (θ_{phys}) with a function that depends on the dimensionality and crystalline structure of interest, e.g. to a range of $0^\circ \le \theta_{phys} < 90^\circ$ for 2-D simple cubic structures or $0^\circ \le \theta_{phys} < 60^\circ$ for 2-D hexagonal structures. We define grain boundaries wherever there is a high gradient in θ_{CD} $(|\nabla\theta_{CD}| > 2.9 \, ^\circ/\text{nm})$.

We update v(T) from the velocity curve given by Burr et. al^{25} to $v_{\infty}(T)$. The two curves are qualitatively similar for $T < T_{melt}$, but $v_{\infty}(T)$ has a higher peak velocity and is also defined for $T > T_{melt}$ (Fig. 3c). We initiate melting at grain boundaries and material interfaces by modifying $Melt_i$:

$$Melt_i = \alpha_{melt} \times v(T) \times (T > T_{melt}) \times CD_i \times HM,$$
 (14)

where HM is 1 at heterogeneous melting sites (grain boundaries and material interfaces) and 0 elsewhere. We modify $stbl_i$ to have a stability valley at $CD \lesssim 1$ when $T > T_{melt}$ to maintain well-defined grains during melt (Fig 5c):

$$stbl_{i} = sign(CD_{i}) \times \alpha_{stbl} \times v(T) \\ \times \begin{pmatrix} (T < T_{melt}) \times pw_{stbl}(sign(CD_{i}) \times CD) \\ + (T > T_{melt}) \times pw_{stbl}(1 - sign(CD_{i}) \times CD) \end{pmatrix} (15)$$

We use the *sign* function (-1/+1/0 for negative/positive/0 arguments, respectively) in (15) to properly call control functions with the non-negative $CD = \sqrt{CD_1^2 + CD_2^2}$ if CD_i becomes negative due to numerical errors. We can control the temperature at which melting begins (T_{melt}), the time required for a liquid layer to form between grains (via α_{melt}), and the melting rate [$\nu(T)$, $T > T_{melt}$] with this framework.

To demonstrate this updated model, we first simulate heterogeneous melting of a polycrystalline 2-D 200 nm square (20 nm out of plane depth) by setting T = 900 K (Fig 6). A liquid layer forms at grain boundaries and around the

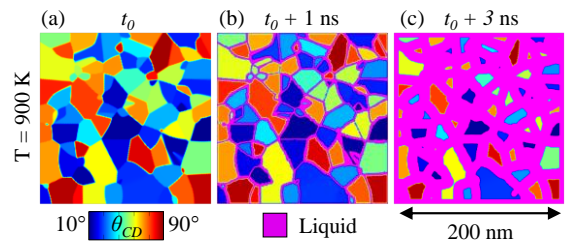


Fig 6. (a) A polycrystalline GST square is brought to 900 K at t_0 . (b) 3 Liquid forms at grain boundaries in 1 ns and (c) melts at 1.3 nm/ns.

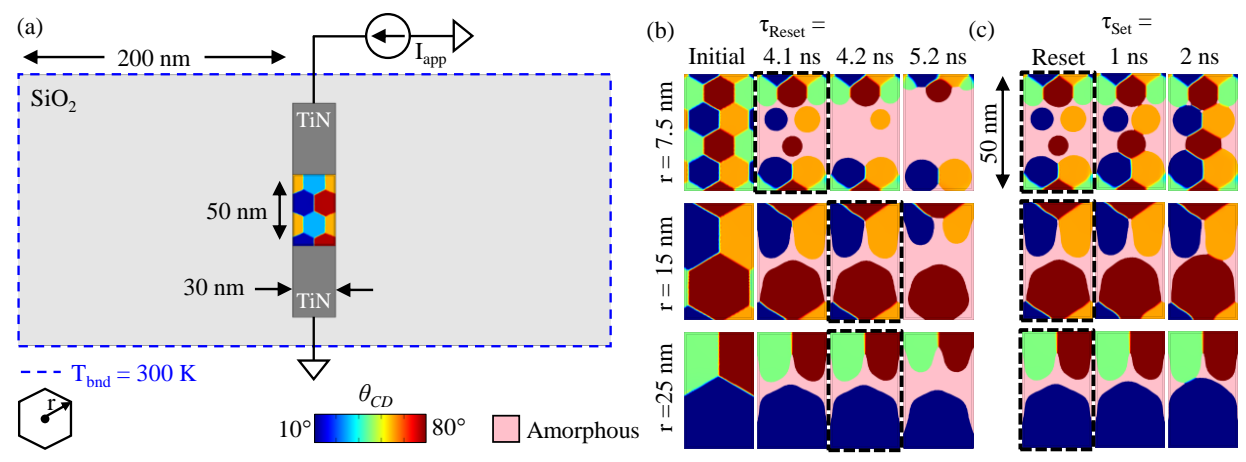


Fig 7. (a) Schematic illustration of geometry and initial and boundary conditions used in simulations. I_{app} is a square pulse with 0.1 ns rise and fall times and a magnitude of 500 μA for reset or 50 μA for set. (b) Crystal maps of initial conditions and after reset with 3 different pulse durations (τ_{Reset}) for 7.5 nm, 15 nm, and 25 nm grains. The amorphous area (and hence reset resistance) increases with τ_{Reset} . The *Initial* column is used for $R_{Initial}$ in Fig 8 and Fig 9. A ~20x increase in cell resistance requires a 4.1 ns reset pulse for 7.5 nm grains and a 4.2 ns reset pulse for 15 nm or 25 nm grains (dashed borders). (c) Quenched-in crystals embedded in the amorphous GST in the r = 7.5 nm case grow simultaneously, allowing for shorter set times.

perimeter in ~1 ns, then grows at $v_{\infty}(900 \text{ K}) \approx 1.3 \text{ nm/ns}$. Next, we simulate electrical cycling of a 30 nm wide confined cell (30 nm out of plane depth). We use a regular array of equally sized grains for the initial crystallinity conditions rather than a random grain map so that we can explicitly define grain size (Fig 7a). We vary the durations of square current pulses with 0.1 ns rise and fall times for reset and set of devices with 7.5 nm, 15 nm, and 25 nm radius grains. The devices achieve a reset resistance increase (R/R_{Initial}) of $>10^2$ in 4.2 ns when r =7.5 nm but require 5.2 ns to reach this contrast when r = 15nm or 25 nm (Fig 7b, Fig 8). We use devices reset to similar R/R_{Initial} for set comparisons. 7.5 nm grains set more quickly due to templated growth from quenched-in crystals when $R/R_{Initial} \approx 20$ (Fig 7c, Fig 9). However, fewer quenched-in crystals remain after stronger resets, increasing the resistance ratio and set times: set is achieved through templated growth from crystalline fronts at the top and bottom contacts. Wang et. al⁸ experimentally showed a trend of decreased reset and set times as radii decreased from 8.5 nm to 5 nm but achieved sub-nanosecond reset while requiring ~50 ns for set. The longer reset and shorter set times in our simulations are consistent with a v_{∞} that underestimates melting velocities but overestimates crystallization velocities, resulting in less melting during reset, more crystallization while cooling after reset, and faster crystallization during set.

In conclusion, we have proposed and studied heterogeneous melting as a mechanism for improved PCM performance as grain size decreases. Smaller grains result in more phase change sites acting simultaneously, decreasing reset and set times. The models presented are for $Ge_2Sb_2Te_5$, but temperature and grain size dependent phase change velocities for other materials can be calculated given the appropriate thermodynamic $(c_{p,l}, c_{p,c}, \Delta h_{lc}(T_x)$, and T_{melt}) and

kinetic $[\eta(T)]$ parameters.

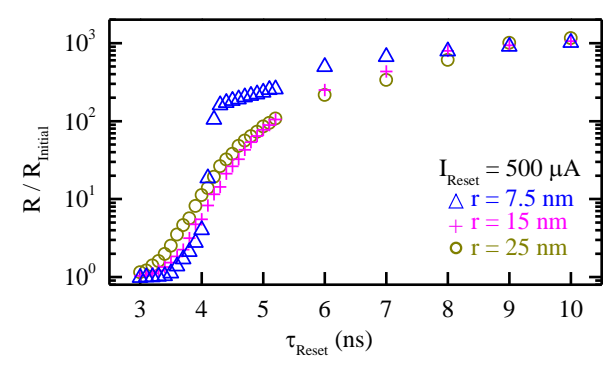


Fig 8. 'Reset' resistance after a square current pulse (500 μA magnitude and $τ_{Reset}$ duration). Smaller grains allow for faster reset, while larger grains have a wider pulse duration window for intermediate values. $R_{Initial}$ corresponds to the cells in the *Initial* column in Fig 7b.

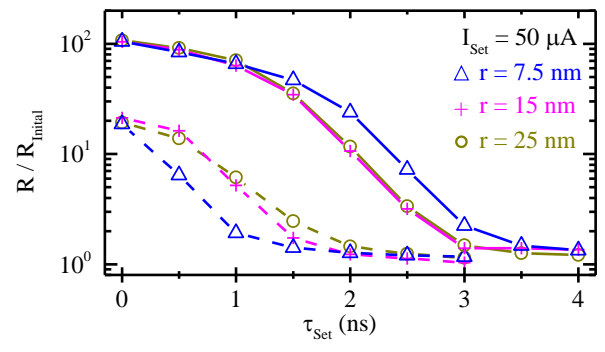


Fig 9. 'Set' resistance after a square current pulse (50 μA magnitude and τ_{Set} duration) beginning with ~20x (dashed lines) and ~100x (solid lines) reset resistances for each grain size (Fig 8). Smaller grains allow for faster set when the initial reset resistance is low. Set time becomes less dependent on grain size as fewer quenched-in crystals remain in the amorphous region and reset resistance increases; crystallization is achieved through templated growth from the same number of similarly spaced crystal-amorphous interfaces. Δ $R_{Initial}$ corresponds to the cells in the Initial column in Fig 7b.

References

- ¹ Q.S. Mei and K. Lu, Prog. Mater. Sci. **52**, 1175 (2007).
- ² Z. Woods and A. Gokirmak, IEEE Trans. Electron Devices **64**, 4466 (2017).
- ³ Z. Woods, J. Scoggin, A. Cywar, L. Adnane, and A. Gokirmak, IEEE Trans. Electron Devices **64**, 4472 (2017).
- ⁴ A. Faraclas, G. Bakan, L. Adnane, F. Dirisaglik, N.E. Williams, A. Gokirmak, and H. Silva, IEEE Trans. Electron Devices **61**, 372 (2014).
- ⁵ H. Silva, A. Faraclas, and A. Gokirmak, in *Nanoscale Semicond. Memories Technol. Appl.*, edited by S. Kurinec and K. Iniewski, 1st ed. (CRC Press, Boca Raton, 2014), pp. 307–332.
- ⁶ F. Dirisaglik, G. Bakan, Z. Jurado, S. Muneer, M. Akbulut, J. Rarey, L. Sullivan, M. Wennberg, A. King, L. Zhang, R. Nowak, C. Lam, H. Silva, and A. Gokirmak, Nanoscale 7, 16625 (2015).
- ⁷ S. Muneer, J. Scoggin, F. Dirisaglik, L. Adnane, A. Cywar, G. Bakan, K. Cil, C. Lam, H. Silva, and A. Gokirmak, AIP Adv. **8**, 065314 (2018).
- ⁸ W.J. Wang, D. Loke, L.T. Law, L.P. Shi, R. Zhao, M.H. Li, L.L. Chen, H.X. Yang, Y.C. Yeo, A.O. Adeyeye, T.C. Chong, and A.L. Lacaita, Tech. Dig. Int. Electron Devices Meet. IEDM 733 (2012).
- ⁹ W. Wang, D. Loke, L. Shi, R. Zhao, H. Yang, L.T. Law, L.T. Ng, K.G. Lim, Y.C. Yeo, T.C. Chong, and A.L. Lacaita, Sci. Rep. **2**, 1 (2012).
- ¹⁰ F. Spaepen, Acta Metall. **23**, 729 (1975).
- ¹¹ F. Spaepen and R.B. Meyer, Scr. Metall. **10**, 37 (1976).
- ¹² F. Spaepen, Mater. Sci. Eng. A **178**, 15 (1994).
- ¹³ Z. Jian, K. Kuribayashi, and W. Jie, Mater. Trans. **43**, 721 (2002).
- ¹⁴ D.T. Wu, L. Gránásy, and F. Spaepen, MRS Bull. **29**, 945 (2004).
- ¹⁵ J. Orava and A.L. Greer, Acta Mater. **139**, 226 (2017).
- ¹⁶ J. Mellenthin, A. Karma, and M. Plapp, Phys. Rev. B Condens. Matter Mater. Phys. **78**, 1 (2008).
- ¹⁷ A.M. Alsayed, M.F. Islam, J. Zhang, P.J. Collings, and A.G. Yodh, Science (80-.). **309**, 1207 (2005).
- ¹⁸ D.R. Uhlmann and E.V. Uhlmann, in *Nucleation Cryst. Liq. Glas.*, edited by M.C. Weinberg (The American Ceramic Society, 1993), pp. 109–140.
- ¹⁹ M.D. Ediger, P. Harrowell, and L. Yu, J. Chem. Phys. **128**, (2008).
- ²⁰ J. Orava, A.L. Greer, B. Gholipour, D.W. Hewak, and C.E. Smith, Nat. Mater. **11**, 279 (2012).
- ²¹ J. Akola and R.O. Jones, Phys. Rev. B Condens. Matter Mater. Phys. **76**, 1 (2007).
- ²² J.A. Kalb, Crystallization Kinetics in Antimony and Tellurium Alloys Used for Phase Change Recording, Ph.D. dissertation. I. Physikalisches Institut der Rheinisch-Westfälische Technische Hochschule (RWTH) Aachen, 52056 Aachen, Germany, 2006.
- ²³ W. Kauzmann, Chem. Rev. **43**, 219 (1948).
- ²⁴ L. Adnane, F. Dirisaglik, A. Cywar, K. Cil, Y. Zhu, C. Lam, A.F.M. Anwar, A. Gokirmak, and H. Silva, J. Appl. Phys. **122**, 125104 (2017).
- ²⁵ G.W. Burr, P. Tchoulfian, T. Topuria, C. Nyffeler, K.

- Virwani, A. Padilla, R.M. Shelby, M. Eskandari, B. Jackson, and B.S. Lee, J. Appl. Phys. **111**, 104308 (2012).
- ²⁶ G. Bakan, N. Khan, H. Silva, and A. Gokirmak, Sci. Rep. **3**, 2724 (2013).
- ²⁷ J. Scoggin, R.S. Khan, H. Silva, and A. Gokirmak, Appl. Phys. Lett. **112**, 193502 (2018).